Medium perturbations of atomic extravalence excitations

Itzhak Messing, Baruch Raz, and Joshua Jortner

Department of Chemistry, Tel-Aviv University, Tel-Aviv, Israel
(Received 13 January 1976)

In this paper we present the results of an experimental study of the lowest $^1S_0 \rightarrow {}^3P_1$ extravalence electronic excitation of atomic xenon in dense supercritical and subcritical fluid argon over the density range 0.1–1.4 g·cm^{-3}, spanning the temperature region 80–300°K. Solvent perturbations were characterized in terms of the spectral shift, the linewidth and the first and the second moments of the absorption band. These energetic parameters exhibit a weak temperature sensitivity and a strong density dependence. The experimental data were analyzed in terms of the semiclassical theory of line broadening extended to account for guest–host and host–host correlations and incorporating realistic pair potentials in the ground and in the excited electronic states. The semiclassical theory results in manageable expressions for the first and for the second moments of the absorption band which are expressed in terms of a difference guest–host interaction potential together with the solute–solvent and the solvent–solvent radial distribution functions. The theory provides a semiquantitative account for the weak temperature dependence and for the marked density dependence of the energetic parameters specifying solvent perturbations and was utilized to extract quite reliable information concerning the excited state $Xe(^3P_1)+Ar(^1S_0)$ potential.

I. INTRODUCTION

There have been extensive experimental spectroscopic studies of the level structure of electronically excited atomic impurity states in solid[1–3] and in liquid[4] rare-gas alloys. The lowest excited impurity state of a guest rare-gas atom in solid insulators corresponds to an intermediate situation between the Wannier scheme[5] and the Frenkel tight-binding picture,[6] and each theoretical model requires gross modifications for a quantitative description of this state.[3] In the modified Wannier scheme[5] large central-cell corrections have to be incorporated. In the modified tight-binding scheme[6] the energy shift of the lowest atomic extravalence excitation relative to the gas phase value originates from a delicate balance between repulsive nonorthogonality terms (contributing to a large positive energy correction) and between charge-transfer and dispersion interactions (which result in a negative energy correction). The former short-range repulsive interactions dominate the energy shift, resulting in a large spectral blue shift relative to the gas phase value.[6] The modified Wannier model[5] is adequate for the correlation of a large number of experimental data regarding the energy of the lowest extravalence excitation of atomic and molecular impurity states in simple molecular solids.[2,3] On the other hand, the tight-binding approach yields a proper rationalization for the large (0.3–1 eV) blue shifts in the absorption spectra of the lowest Rydberg state of atomic and molecular impurity states[1–3] in solid and liquid rare gases, and once medium relaxation effects[3,7] are incorporated an adequate qualitative rationalization for the small spectral shift (i.e., a large Stokes shift) in emission for such impurity states[7] can be provided. The quantitative application of the modified tight-binding scheme is fraught with considerable difficulties, as reliable quantum mechanical calculations of the interatomic interactions between the electronically excited guest and the ground state host are not yet available. An obvious way out of this difficulty is to incorporate all the relevant interactions into semiempirical guest–host pair potentials. One can then hope to be able to account for medium perturbations of extravalence excitations of a guest atom in a dense host fluid over a broad density range, a problem which constitutes the subject matter of the present paper. For the case of spectral perturbations at low density, one can apply the statistical theory[8–10] of line broadening to account for spectral shifts and for the appearance of satellite bands,[10] while at higher densities the statistical theory has to be extended to account for pair and higher correlation effects between the positions of the perturbing atoms.[10] Such an approach has been widely applied for the study of spectral perturbations of alkali atoms.[9,10] Roncin[11] has proposed that excited state interatomic potentials may be estimated from spectral shifts of impurity states in solid rare gases assuming substitutional disorder.[12] Roncin's model can account only for spectral shifts, but not for the appreciable line broadening experimentally observed in the medium perturbed guest spectra, as his formalism results in a delta function for the absorption line shape. In a recent important contribution to this field, Saxton and Deutch[13] have used the (blue) solvent shifts in the absorption spectra of Xe/Ar dense gaseous mixtures at moderate ($\rho \cong 0.5$ g cm^{-3}) densities to obtain the excited state $Xe(^3P_1)+Ar(^1S_0)$ potential,[14] which together with a scaled radial distribution function was utilized to evaluate the absorption and the emission shifts of Xe in liquid Ar. Subsequently, the present authors[15] have applied the statistical model[8–10] to extract information concerning the excited state $Xe(^3P_1)+Ar(^1S_0)$ potential.

In this paper we present the results of an experimental study of the vacuum ultraviolet spectra of the lowest Xe resonance line in dense Ar fluid from 50 atm to the liquid density over the temperature range 80–300 °K, spanning the density region of 0.1–1.4 g cm^{-3} (see Fig. 1). A preliminary report of the absorption spectra of the Xe/Ar system has been already published.[15] Here we present an extended account of our recent experimental data and their theoretical analysis in terms of the statistical theory.

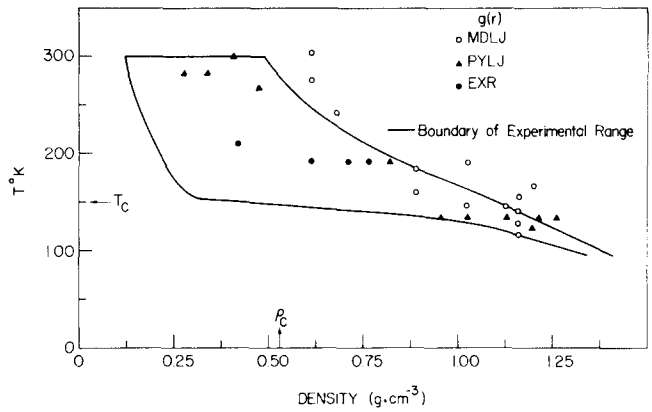

FIG. 1. A schematic representation of the range of the available experimental data and theoretical input information for the Xe/Ar system. Experimental spectroscopic measurements were conducted in the ρ–T range enclosed by heavy lines. Radial distribution functions $g(r)$ for a pure fluid utilized for the calculations of spectral perturbations are designated by dots. o: $g(r)$ from molecular dynamics with a Lennard-Jones potential (Ref. 29); ▲: $g(r)$ from the Percus–Yevick approximation with a Lennard-Jones potential (Ref. 30); ●: $g(r)$ from x-ray scattering data (Ref. 31). ρ_c and T_c represent the critical density and the critical temperature of Ar, respectively.

II. EXPERIMENTAL PROCEDURES

A. Spectroscopic techniques

The absorption spectra of gaseous and liquid Xe/Ar mixtures were monitored in the spectral region 1600–1300 Å utilizing the experimental setup schematically presented in Fig. 2. A conventional Tanaka light source[16] (Kr lamp) was employed. We have used a McPherson 0.3 Czerny-Turner vacuum spectrograph equipped with a grating of 2400 lines/mm. The resolution for 100 μm slit width was 1.0 Å (50 cm^{-1}). A homemade double-beam recording system was constructed using a static beam splitter and two EMI 9514S photomultipliers coated with sodium salicylate converter. The signal detecting system consisted of a two-channel amplifier and a recorder.

B. Absorption cell

The cell for high pressure work (Fig. 3) consists of an optical cell connected to a sample mixing chamber. The optical cell was constructed from a stainless steel cylindrical block (length 1 cm, diam 5 mm). The optical windows consisted of 5 mm thick MgF_2 windows which were sealed into stainless steel frames with the aid of indium rings. These frames were sealed to the cell (see Fig. 4) by pressing their conical surface onto a right angle edge inside the cell. The optical cell was equipped with a stainless steel cooling coil for liquid N_2 cooling, a heating element, and a Cu/Cu:Co thermocouple. The temperature of the optical cell could be varied in the range 80–300 °K with an accuracy of ± 1 °K. A small stainless steel cylinder (volume 10 cm^3) connected to the optical cell (see Fig. 3) by a 2 mm diam stainless steel pipe serves as the sample mixing chamber. The cell was connected to the gas handling system by a stainless steel pipe and a high pressure valve. The absorption cell could be operated in the pressure range 10^{-8}–400 atm over a broad temperature range (80–300 °K).

C. Sample preparation

The cell (total volume 12.5 cm^3) was connected to the gas handling system (volume 3000 cm^3). Xe at pressures 0.05–0.15 torr contained in the gas handling system was deposited in the cylinder at 77 °K. Subsequently, gaseous Ar (Matheson Research Grade) at known pressure (0.1–1.5 atm) is accumulated from the gas mixing system (maintained at room temperature) into the cylinder which was cooled to 77 °K. The high pressure valve was then closed and the mixture contained in the closed cell was allowed to equilibrate at room temperature. The highest pressure obtained by this method, $P = 400$ atm at $T = 300$ °K, was restricted by the mechanical strength of the MgF_2 windows. The initial Xe concentration was ~ 1 ppm.

D. Density determination

The optical cell (volume $v = 1.7$ cm^3) was maintained at the temperature T while the cylinder and the con-

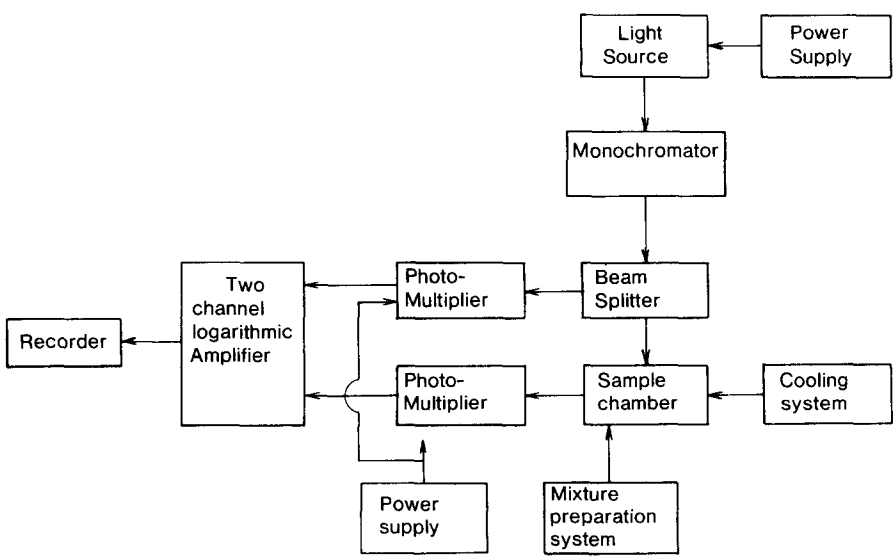

FIG. 2. A block diagram of the experimental setup.

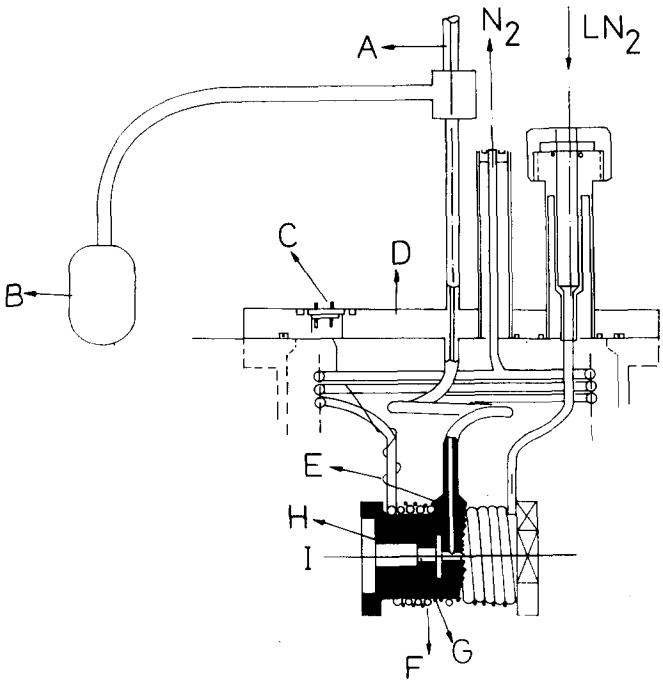

FIG. 3. The absorption cell for high pressure vacuum ultraviolet work. A: Pipe leading to the gas handling system. B: Sample mixing chamber. C: Electrical feed-through. D: Vacuum chamber cover flange. E: Thermocouple. F: Cooling coil. G: Heating element. H: Closing nut. I: Optical axis.

necting tube (volume $v_2 = 10.8$ cm^3) were kept at room temperature. In each experiment we have determined the total mass of the Ar contained in the cell. In the supercritical region the density ρ inside the optical cell was then determined (assuming that the pressure is uniform throughout the cell) from the simple relation $\rho = (n - \rho_2 v_2)/v$, where ρ_2 is the gas density in the volume v_2, utilizing[17] the ρ–P isotherms of ^{18}Ar at room temperature and at T. Most of our data were obtained in the supercritical region. In the subcritical region the liquid density is given by its equilibrium value.[18]

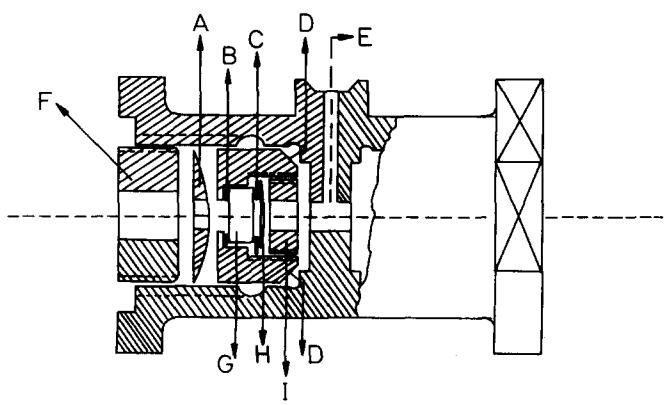

FIG. 4. The Window Sealing Method. A: Steel spring. B: Indium ring. C: Teflon ring. D: Stainless steel frame, (conically edged). E: Gas inlet. F: Closing nut. G: MgF_2 window. H: Steel spring. I: Closing nut.

III. SOLVENT PERTURBATIONS OF Xe($^3P_1$) IN DENSE Ar

In Fig. 5 we present the absorption spectra of dilute Xe/Ar mixture ([Xe]/[Ar] $\cong 10^{-6}$) over the density range

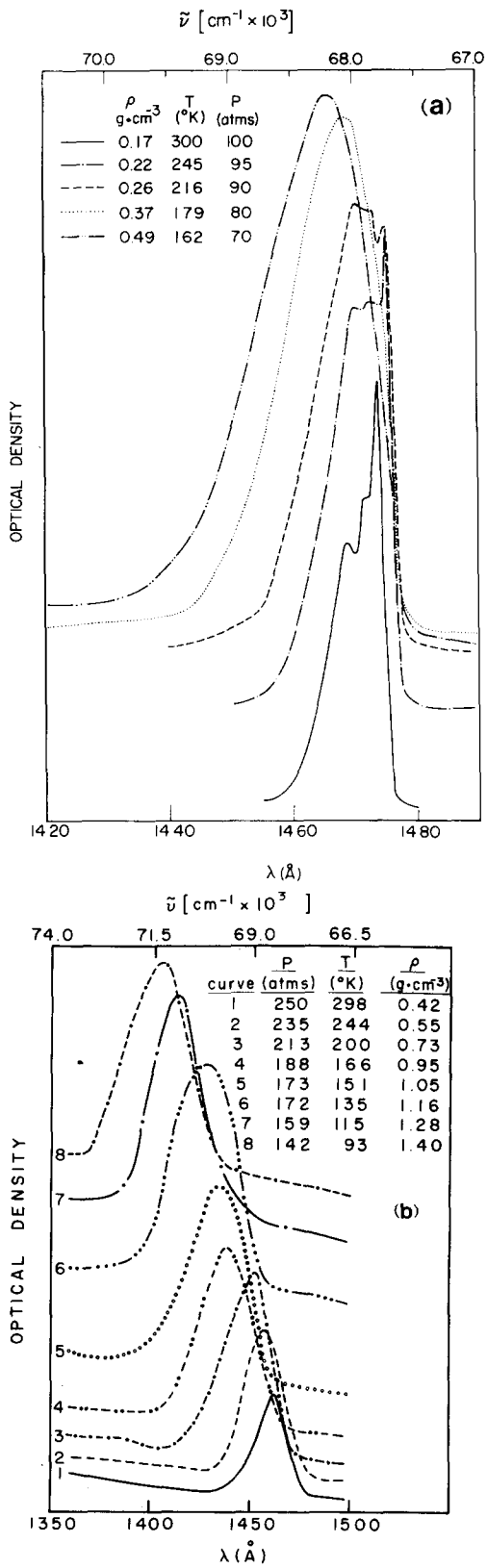

FIG. 5. Absorption spectra of the Xe $^1S_0 \rightarrow {}^3P_1$ transition perturbed by Ar. (a) Density range $\rho = 0.1$–0.5 g·cm^{-3}. (b) Density range $\rho = 0.4$–1.4 g·cm^{-3}.

$\rho = 0.05-1.4$ g cm^{-3} and over the temperature range $T = 80-300$ °K. At moderately low Ar densities, $\rho \leq 0.2$ g cm^{-3}, these spectra exhibit the well-known[19,20] two blue satellites, i.e., extra absorption bands appearing [Fig. 5(a)] on the high energy side of the (perturbed) Xe($^3P_1$) resonance line, which originate from bound-continuum and from continuum-continuum transitions between the nuclear states of the Xe/Ar pair. The intensities of the two satellite bands are proportional to the product of the number densities of the Xe and Ar atoms[20] in accord with their assignment to the absorption of a guest-host pair. At higher ($\rho \cong 0.3$ g cm^{-3}) Ar density the intensity of the satellite hands exceeds that of the resonance line and at $\rho > 0.3$ g cm^{-3} the absorption spectrum merges into a single broad absorption band, in agreement with the previous observation of Rupin *et al.*[21] From the absorption spectra, we have determined the following energetic parameters (Figs. 6 and 7) specifying the medium induced perturbation of the Xe($^3P_1$) state: (1) the spectral shift Δ of the maximum of the absorption line relative to the atomic value $\hbar\omega_0$. It is gratifying to note that our data for Δ at $T = 290$ °K over the density range 0.05–0.6 g cm^{-3} are in good agreement (within the experimental uncertainty claimed by us) with the room temperature data of Rupin *et al.*,[21] which were reproduced in Fig. 6(a), while our data for $\rho = 1.4$ g cm^{-3} and $T = 85$ °K agree with previous results for liquid Xe/Ar obtained in this laboratory[4]; (2) the first moment M_1 of the absorption band relative to $\hbar\omega_0$

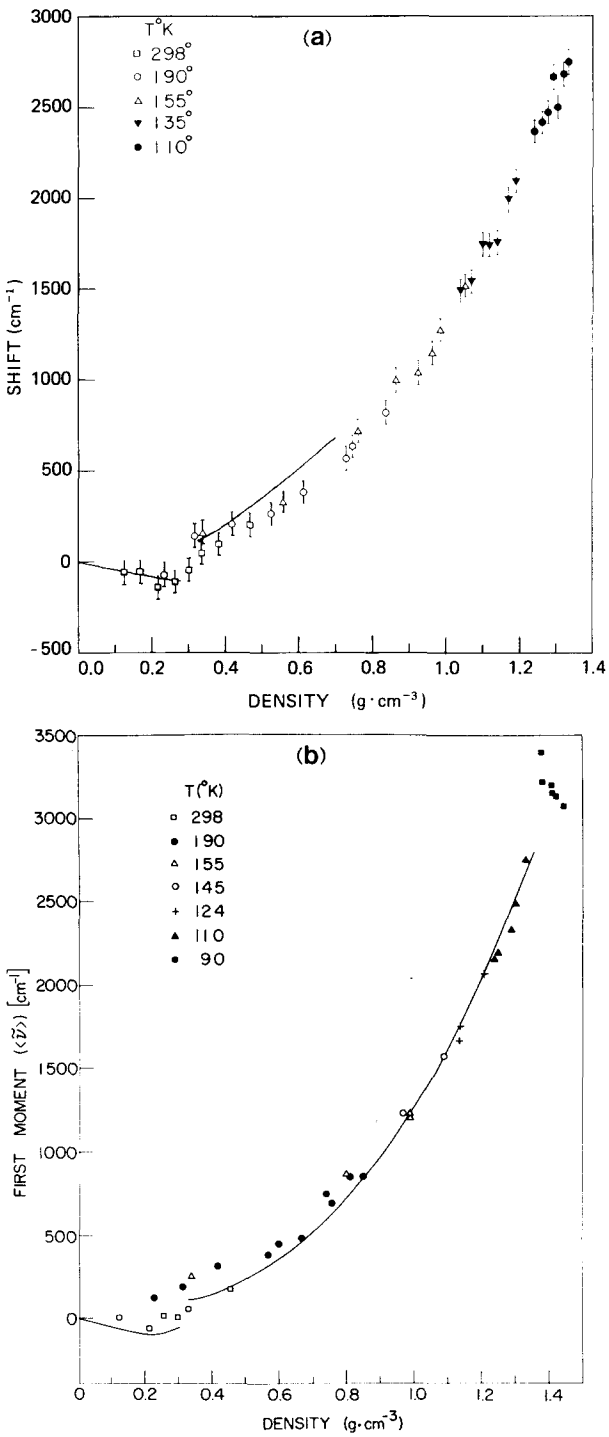

FIG. 6. (a) Density dependence (in the temperature range 90–300 °K) of the spectral shift of the maximum of the absorption line relative to the atomic value $\hbar\omega_0 = 68\,050$ cm^{-1}. In the density range $\rho < 0.3$ g · cm^{-3}, where satellite bands are resolved the maximum of the (perturbed) resonance, i.e. the low energy band was taken. The solid curve represents the room temperature data of Rupin *et al.* (Ref. 21). (b) Density dependence in the temperature range 90–300 °K of the first moment of the absorption band. The solid curve represents the (average) spectral shift.

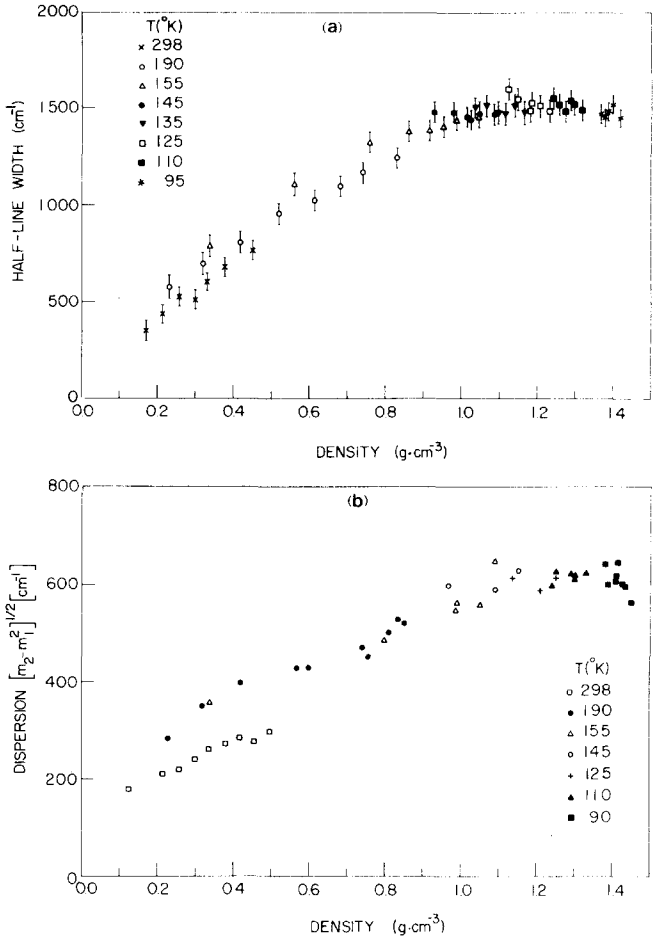

FIG. 7. (a) Density dependence over the temperature range 90–300 °K of the linewidth at half maximum. (b) Density dependence over the temperature range 90–300 °K of the dispersion of the absorption line.

$$M_1 = \int \mathfrak{L}(E) E\, dE \Big/ \int \mathfrak{L}(E)\, dE \ , \tag{3.1}$$

where $\mathfrak{L}(E)$ is the absorption coefficient at energy $E = \hbar\omega - \hbar\omega_0$; (3) the width δ at half-maximum; (4) the dispersion M_2,

$$M_2 = \left[\int \mathfrak{L}(E) E^2\, dE \Big/ \int \mathfrak{L}(E)\, dE - M_1^2 \right]^{1/2} \tag{3.2}$$

of the absorption band.

The following general features of these results should be noted. First, the energetic parameters characterizing the medium perturbations exhibit a considerable density dependence, but only a weak temperature sensitivity. Δ and M_1 are practically temperature independent, as evident from Figs. 6(a) and 6(b), while δ and M_2 at lower densities ($\rho = 0.2$–0.4 g cm^{-3}) reveal a slight decrease at 290 °K relative to the low temperature (90–190 °K) data, while for higher densities ($\rho > 0.4$ g cm^{-3}) δ and M_2 are again practically independent of T [Figs. 7(a), 7(b)]. Second, at low densities ($\rho \leq 0.2$ g cm^{-3}) red spectral shifts of the resonance line are observed, indicating the major role of dispersion interaction in this density range, while at higher densities ($\rho > 0.3$ g cm^{-3}) $\Delta > 0$ and the spectral shift is dominated by repulsive interactions. Third, regarding the general trend of the density dependence of the spectral parameters, we notice that for $\rho > 0.3$ g cm^{-3} Δ (and M_1) increase with increasing ρ, exhibiting a superlinear density dependence. In the density range $\rho = 0.3$–0.9 g cm^{-3} δ and M_2 increase approximately linearly with increasing ρ and reveal a weak density dependence in the range $\rho = 0.9$–1.4 g cm^{-3}. Fourth, at low densities ($\rho = 0.2$–0.4 g cm^{-3}) the absorption line shapes are asymmetric tailing towards high energies and $\Delta < M_1$ as evident from Fig. 6(b). In the high density range $\rho = 0.4$–1.4 g cm^{-3} the line shapes are symmetrical and, within experimental uncertainty, $\Delta = M_1$. Furthermore, in the high density range $\delta \approx (2.5 \pm 0.1) M_2$ and the second moment of the intensity distribution is close to that corresponding to a Gaussian distribution, where $\delta = 2.35\, M_2$.

IV. STATISTICAL THEORY OF LINE SHAPES

The most interesting feature of solvent perturbation of the Xe($^3P_1$) line by Ar($^1S_0$) involves the dominating role of guest–host short range repulsive interactions in determining the blue spectral shift. Saxton and Deutch[13] have accounted for the result by the application of the statistical theory of line broadening. In view of the sparse experimental information available to them, moderate density data, $\rho \approx 0.5$ g cm^{-3}, have been utilized to determine Δ, which was identified with M_1. It is interesting to attempt to provide a more detailed picture of the spectral perturbations accounting not only for the spectral shifts but also for line broadening. In what follows we shall consider solvent perturbation in the Xe($^3P_1$) + Ar($^1S_0$) system applying Margenau's[8] statistical theory extended to account for more realistic interaction potential functions and for guest–host and host–host correlation. This semiclassical theory results in an expression for the absorption line shape which is determined by the guest–host interaction potentials and the (multiparticle) probability distribution function of the fluid.[10] It is of some interest to relate the extended statistical theory[10,22] to the general formalism of line broadening in solids,[23,24] and we proceed first to present a brief review of this approach which rests on the semiclassical formalism of the Franck–Condon principle. Let $W_g(\mathbf{R}_1, \mathbf{R}_2 \ldots \mathbf{R}_N)$ and $W_e(\mathbf{R}_1, \mathbf{R}_2 \ldots \mathbf{R}_N)$ denote the multidimensional adiabatic potential surfaces of the system in the ground and in the electronically excited state, respectively. The guest atom is located at the origin, while $\mathbf{R}_1, \mathbf{R}_2 \ldots \mathbf{R}_N$ represent the position vectors of the perturbing atoms. Kubo and Toyozawa[23] and Lax[24] have demonstrated that in the high temperature limit, a closed expression for the line shape $\mathfrak{L}(E)$ can be derived for a general form of the nuclear potentials. The high temperature limit is realized when the variation of the potential energy in the the initial state within the averaged de Broglie wavelength $\hbar/(\mu k_B T)^{1/2}$ is negligible relative to the thermal energy $\beta^{-1} = k_B T$, so that

$$\beta \left[\hbar \Big/ (\mu k_B T)^{1/2} \frac{\partial}{\partial \mathbf{R}_i} \right]^n W_g \ll 1 \tag{4.1}$$

for all $\mathbf{R}_i$. The line shape function for an allowed optical transition[23] is

$$\mathfrak{L}(\hbar\omega) = Z^{-1} \int \cdots \int \exp[-\beta W_g(\mathbf{R}_1 \ldots \mathbf{R}_N)] \times \delta[W_g(\mathbf{R}_1 \ldots \mathbf{R}_N) - W_e(\mathbf{R}_1 \ldots \mathbf{R}_N) + \hbar\omega - \hbar\omega_0] \prod_i d^3 R_i \ , \tag{4.2a}$$

$$Z = \int \cdots \int \exp[-\beta W_g(\mathbf{R}_1 \ldots \mathbf{R}_N)] \prod_i d^3 R_i \ , \tag{4.2b}$$

where $\hbar\omega$ is the photon energy while $\hbar\omega_0$ corresponds to the guest atomic excitation at $\rho = 0$. Next, one has to invoke the additivity assumptions for the potential surfaces which are thus approximated as superpositions of pair potentials

$$W_g(\mathbf{R}_1 \ldots \mathbf{R}_N) = \sum_i V_g(\mathbf{R}_i) + \sum_{i<m} U_g(|\mathbf{R}_i - \mathbf{R}_m|) \ , \qquad W_e(\mathbf{R}_1 \ldots \mathbf{R}_N) = \sum_i V_e(\mathbf{R}_i) + \sum_{i<m} U_g(|\mathbf{R}_i - \mathbf{R}_m|) \ . \tag{4.3}$$

$V_g(\mathbf{R}_i)$ and $V_e(\mathbf{R}_i)$ are the Xe–Ar pair potentials, the Xe atom being in the ground and in the excited state, respectively, while $U_g(|\mathbf{R}_i - \mathbf{R}_m|)$ corresponds to the Ar–Ar pair potential. The difference guest–host pair potential is defined as

$$\Delta V(\mathbf{R}_i) = V_e(\mathbf{R}_i) - V_g(\mathbf{R}_i) \ . \tag{4.4}$$

From Eqs. (4.2)–(4.4) the line shape is recast in terms of a Fourier transform

$$\mathfrak{L}(\hbar\omega) = \frac{1}{2\pi} \int_{-\infty}^{\infty} dt \exp[i\hbar(\omega - \omega_0)t] f(t) \tag{4.5}$$

where the generating function is

$$f(t) = \int \cdots \int P(\mathbf{R}_1, \mathbf{R}_2 \ldots \mathbf{R}_N) \exp\left[-i \sum_i \Delta V(\mathbf{R}_i) t \right] \prod_i d^3 R_i \ . \tag{4.6}$$

$P(\mathbf{R}_1 \ldots \mathbf{R}_N)$ is the probability that one perturbing atom is at $\mathbf{R}_1$, a second atom at $\mathbf{R}_2$, etc.,

$$P(\mathbf{R}_1, \mathbf{R}_2 \ldots \mathbf{R}_N) = \frac{\exp[-\beta W_s(\mathbf{R}_1, \mathbf{R}_2 \ldots \mathbf{R}_N)}{Z} \quad . \tag{4.7}$$

Equation (4.6) was originally presented by Mahan[10] who has applied the functional derivative method[25] for a classical fluid to express the generating function Eq. (4.6) in terms of an exponential density expansion[10a,25]

$$\ln f(t) = A_1(t) + A_2(t) + \cdots \quad , \tag{4.8a}$$

where the lowest terms are

$$A_1(t) = \int d^3R_1 \mathfrak{F}_1(\mathbf{R}_1)[\exp(-i\Delta V(\mathbf{R}_1)t) - 1]$$

$$A_2(t) = \tfrac{1}{2}\int\int d^3R_1 d^3R_2 \mathfrak{F}_2(\mathbf{R}_1, \mathbf{R}_2) \tag{4.8b}$$

$$\times[\exp(-i\Delta V(\mathbf{R}_1)t) - 1][\exp(-i\Delta V(\mathbf{R}_2)t) - 1],$$

and the general term is

$$A_n(t) = \frac{1}{n!}\int \cdots \int \prod_{j=1}^{n} d^3R_j \mathfrak{F}_n(\mathbf{R}_1 \ldots \mathbf{R}_n)$$

$$\times \prod_{j=1}^{n}[\exp(-i\Delta V(\mathbf{R}_j)t) - 1] \, , \tag{4.8c}$$

and $\mathfrak{F}_n(\mathbf{R}_1 \ldots \mathbf{R}_n)$ corresponds to the Ursell distribution function.[25]

Equations (4.5) and (4.8) for the absorption line shape are expected to be valid for a strongly allowed transition of a guest atom in a system where the semiclassical approximation, Eq. (4.1), for nuclear motion is valid, and where the medium can be treated as a classical fluid. We are concerned here with medium perturbations of an allowed $Xe(^1S_0 \rightarrow {}^3P_1)$ transition by a classical Ar fluid. The semiclassical approximation (Eq. 4.2) is perfectly adequate as vibrational $k_BT \geq 70$ cm^{-1}, while the effective frequencies for the ground state Ar–Ar and Ar–Xe pairs are $h\nu \simeq 10$ cm^{-1}, whereupon $h\nu \ll k_BT$, which provides a special case of the validity condition [Eq. (4.1)] for $n = 2$. We can apply the semiclassical formalism with confidence to the problem at hand.

This theory, which constitutes a complete semiclassical analogy of electron–phonon coupling in solids[23,24] expresses all the relevant information concerning the liquid structure in terms of the Ursell distribution functions. $\mathfrak{F}_1(\mathbf{R}_1)$, appearing in Eq. (4.8b) is expressed in the well-known form[25]

$$\mathfrak{F}_1(\mathbf{R}) = \rho g_{12}(\mathbf{R}) \, , \tag{4.9}$$

where $g_{12}(\mathbf{R})$ is the solute–solvent radial distribution function (RDF). $\mathfrak{F}_2(\mathbf{R}_1, \mathbf{R}_2)$, Eq. (4.8b), can be estimated using Kirkwood's superposition approximation,[26]

$$\mathfrak{F}_2(\mathbf{R}_1, \mathbf{R}_2) = \rho^2[g_{11}(|\mathbf{R}_1 - \mathbf{R}_2|) - 1]g_{12}(\mathbf{R}_1)g_{12}(\mathbf{R}_2) \tag{4.10}$$

where $g_{11}(\mathbf{R})$ is the solvent–solvent RDF. Equations (4.9) and (4.10) can be used for the exact evaluation of the first term and for the approximate estimate of the second term in Eq. (4.8a),

$$A_1(t) = 4\pi\rho\int_0^\infty dr\, r^2 g_{12}(r)[\exp(-it\Delta V(r)) - 1] \, , \tag{4.10a}$$

$$A_2(t) = 4\pi\rho^2 \int_0^\infty dr_1\, r_1^2 g_{12}(r_1)[\exp(-it\Delta V(r_1)) - 1]$$

$$\times \int_0^\infty dr_2\, r_2^2 g_{12}(r_2)[\exp(-it\Delta V(r_2)) - 1]\frac{1}{r_1 r_2}$$

$$\times \int_{|r_1 - r_2|}^{|r_1 + r_2|} s[g_{11}(s) - 1]ds \, . \tag{4.10b}$$

It has been a common practice[10,22] to keep only the first term on the right hand side of Eq. (4.8a), a procedure valid for sufficiently low densities when $A_2(t)/A_1(t) \ll 1$. We are interested in the line shape over a wide density range which have to include high order positional correlation effects involving the $\mathfrak{F}_i(\mathbf{R}_1 \ldots \mathbf{R}_i)$ functions of high order. Unfortunately, there is little point in approximating these functions for $i \geq 3$ in terms of the superposition approximation. To overcome this difficulty, we adopt the common method of moment analysis of the line shape function.[10b,10c,23,24] It can easily be demonstrated that the Ith moment of $\mathfrak{L}(E)$

$$m_I = \int \mathfrak{L}(E)E^I dE \tag{4.11}$$

is determined by the Ursell correlation functions up to the Ith order. These moments of the spectral distribution are given in the general form

$$m_I = \left(\frac{1}{i}\right)^I \frac{\partial^I f(t)}{\partial t^I}\bigg|_{t=0} \, . \tag{4.12}$$

The lowest moments of the line shape are obtained from Eqs. (4.8) and (4.10),

$$m_0 = 1 \, , \tag{4.13a}$$

$$m_1 = 4\pi\rho\int_0^\infty dr\, r^2 g_{12}(r)\Delta V(r) \, , \tag{4.13b}$$

$$m_2 = m_1^2 + 4\pi\rho\int dr\, r^2 g_{12}(r)[\Delta V(r)]^2$$

$$+ 8\pi^2\rho^2 \int_0^\infty dr_1\, r_1^2 g_{12}(r_1)\Delta V(r_1)\int_0^\infty dr_2\, r_2^2 g_{12}(r_2)\Delta V(r_2)$$

$$\times \left(\frac{1}{r_1 r_2}\right)\int_{|r_1 - r_2|}^{|r_1 + r_2|} s[g_{11}(s) - 1]ds \, . \tag{4.13c}$$

The experimental first moment and spectral dispersion defined in Sec. III are thus $M_1 = m_1$ and $M_2 = (m_2 - m_1^2)^{1/2}$. As it was pointed out by Margenau[8b] and by Saxton and Deutch[13] the first moment is determined by the difference potential and by the guest–host RDF. M_1 can be utilized to extract relevant information concerning the excited state pair potential or, alternatively, once $\Delta V(r)$ is established M_1 can be used[13] to obtain information on the solution pair RDF. Within the framework of the superposition approximation M_2 is determined by $\Delta V(r)$ and by the solvent–solute and solvent–solvent RDF's. Furthermore, one should note that dynamical corrections, which are neglected in the semiclassical approximation, do not appear in the accurate expression for[10b,24] M_2. The role of three-body correlations on M_2 is incorporated in the third term of the right-hand side of Eq. (4.13c), which is proportional to ρ^2. We have conducted numerical calculations of M_2 in the Xe/Ar system using the approximate difference potential of the form previously used by us[15] together with the Percus–Yevick hard sphere RDF's[27,28] $g_{12}(r)$ and $g_{11}(r)$.

In the density range $\rho < 0.4$ g·cm^{-3} the role of three-body correlations on M_2 is small, less than 5%, while at $\rho = 1.0$ g·cm^{-3} they contribute about 25% to M_2. It is also interesting to note (see Fig. 8) that the contribution of the three-body term to M_2 is negative.

V. RADIAL DISTRIBUTION FUNCTIONS AND EXCITED-STATE POTENTIAL

In order to compute the first moment and the dispersion of the absorption line shape, it is necessary to know the difference potential ΔV, the guest–host RDF, $g_{12}(r)$, and the RDF $g_{11}(r)$ for the pure solvent.

We shall consider first the available information concerning the RDF's for pure liquid Ar. The following types of RDF are available (see Fig. 1) at some temperatures and densities:

(a) $g(r)$ computed by molecular dynamics method with a Lennard-Jones potential[29]; (MDLJ).

(b) $g(r)$ computed by Percus–Yevick approximation with a Lennard-Jones potential[30]; (PYLJ).

(c) $g(r)$ taken from x-ray scattering data[31]; (EXR).

(d) $g(r)$ for hard-spheres mixtures (PYHS) in the Percus–Yevick approximation.[28]

The RDF $g_{12}(r)$ for solvent-solute was estimated from the three, (a), (b) and (c), RDF's for pure fluid given above, using a simple scaling method advanced by Saxton and Deutch[13]:

$$g_{12}(r, T, \rho) = \frac{g(r, T^*, \rho^*)}{g^{HS}(r, \rho^*_{HS})}\, g^{HS}_{12}(r, \rho^*_{HS}) , \qquad (5.1)$$

where $g_{12}(r, T, \rho)$ is the solvent–solute RDF for the Lennard-Jones two-component mixture at temperature T and density ρ. $g(r, T^*, \rho^*)$ is the RDF for a pure Lennard-Jones fluid at the reduced temperature $T^* = k_B T/\epsilon_{12}$ and reduced density $\rho^* = \rho\sigma_{12}^3$, where $\sigma_{12} = 3.65$ Å and $\epsilon_{12} = 0.0153$ eV are the parameters for the ground state Xe/Ar potential.[32] $g^{HS}(r, \rho^*_{HS})$ is the PYHS RDF of a hypothetical hard sphere fluid with a hard sphere radius σ_{12}, and reduced density[27] $\rho^*_{HS} = \rho^*$. Finally, $g^{HS}_{12}(r, \rho^*_{HS})$ is the solute–solvent RDF with hard sphere radii σ_{11} and σ_{22} corresponding to the hard sphere radii of Xe and of Ar, respectively, and at reduced density ρ^*_{HS}. By this scaling method[13] we have derived the MDLJ, PYLJ, and EXR two-component RDF's. In addition, we have utilized the PYHS for a two-component hard sphere mixture RDF calculated in the Percus–Yevick approximation.[28]

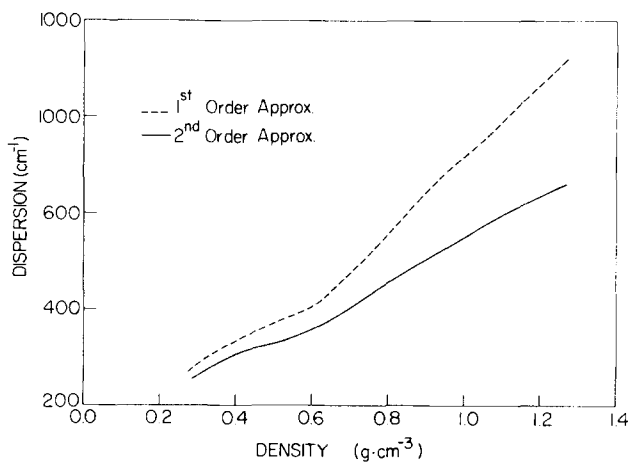

FIG. 8. Model calculations on the effect of three-body correlation effects on the dispersion of the absorption band in the density range 0.3–1.4 g·cm^{-3}. The dashed curve represents M_2 calculated including pair correlations [using only the second termon the rhs of Eq. (4.13c)], while the solid curve is the result incorporating two-body and three-body correlations [using Eq. (4.13c)]. $\Delta V(r)$ is obtained from Eqs. (5.2) and (5.3) with the excited state parameters: $\epsilon = 8\times10^{-3}$ eV; $r_e = 4.65$ Å; $\alpha = 15$. $g_{11}(r)$ is the PYHS (Ref. 27) RDF. $g_{12}(r)$ is a scaled [see Eq. (5.1)] PYLJ (Ref. 30) RDF.

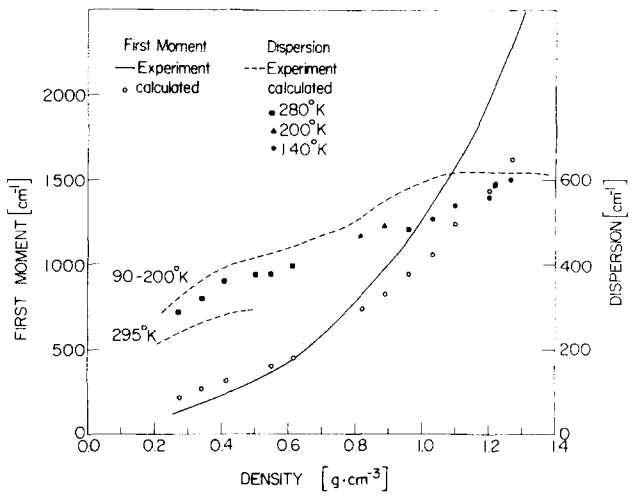

FIG. 9. Density dependence of the first moment (open circles) and of the spectral dispersion (closed points) calculated using a Lennard-Jones excited state potential with $\bar{\sigma}_{12} = 4.13$ Å and $\bar{\epsilon}_{12} = 0.008$ eV and PYLJ RDF's at 140, 200, and 280 °K for the entire density range. The solid curve represents the (temperature averaged) experimental M_1 data while the two dashed curves represent the experimental M_2 values at room temperature and in the temperature range 90–200 °K.

For the ground state Xe($^1S_0$)–Ar potential we have taken the Lennard-Jones (LJ) curve

$$V_g(r) = 4\epsilon_{12}[(\sigma_{12}/r)^{12} - (\sigma_{12}/r)^6] \qquad (5.2)$$

with the parameters[32] $\epsilon_{12} = 0.0153$ eV and $\sigma_{12} = 3.65$ Å. We have attempted to adopt the form of the excited state potential suggested by Saxton and Deutch[13] assuming an LJ potential for the Xe($^3P_1$) + Ar interaction and calculating both the first moment and the dispersion over a wide (0.3–1.4 g·cm^{-3}) density range. The parameters $\bar{\epsilon}_{12}$ and $\bar{\sigma}_{12}$ for the LJ excited state potential were determined by a simultaneous fit of the first moment and the dispersion, Eq. (4.13), to the experimental data in the density range 0.45–0.65 g·cm^{-3}, using scaled PYLJ RDF's. This procedure resulted in the parameters $\bar{\sigma}_{12} = 4.13 \pm 0.03$ Å and $\bar{\epsilon}_{12} = 0.008 \pm 0.002$ eV. The value obtained herein for $\bar{\sigma}_{12}$ is identical with the result of Saxton and Deutch[13]; however, our value for $\bar{\epsilon}_{12}$ is smaller than their estimate ($\bar{\epsilon}_{12} \simeq 0.05$–$0.02$ eV). In Fig. 9 we present the density dependence of M_1 and M_2 calculated from the PYLJ RDF's and LJ potentials, both for the ground and the excited state

pair interaction. Agreement between theory and experiment is reasonable, demonstrating that the statistical theory is adequate to provide a semiquantitative account not only for the first moment but also for the line broadening. It should be noted, however, that the fit of the experimental data (Fig. 9) utilizing the LJ excited state potential is not entirely satisfactory. The experimental values of M_1 exhibit a large systematic deviation (30%–40%) from theory in the high ($\rho = 0.8 - 1.4$ g·cm^{-3}) density range, while the experimental M_2 values are systematically too high (by 10%–15%) throughout the high density range. Such deviations may reflect either the inaccuracy of the scaling approximation, Eq. (5.1), or the inapplicability of the excited state LJ potential. To explore the effect of the functional form of the excited state potential on spectral perturbations, we have decided to use for the sake of more extensive calculation, a pair potential which is characterized by an exponential repulsive part. From the foregoing analysis using LJ potentials for ground and excited state potentials it is apparent that $\bar{\sigma}_{12}$ considerably exceeds σ_{12}, as expected for an extravalence excitation, whereupon the distance dependence of the repulsive interaction is crucial in determining the spectral characteristics. An exponential repulsive interaction was found to be superior to the r^{-12} form in fitting the spectral data. A satisfactory fit of the M_1 and M_2 data over a broad density range was accomplished by choosing an exponential-6 three-parameter potential of the form

$$V(r) = \epsilon \left(1 - \frac{6}{\alpha}\right)^{-1} \left\{ \left(\frac{6}{\alpha}\right) \exp\left[\alpha\left(1 - \frac{r}{r_e}\right)\right] - \left(\frac{r_e}{r}\right)^6 \right\} , \qquad (5.3)$$

where ϵ is the potential well depth, r_e is the equilibrium distance, and α is a steepness parameter.

Numerical results indicate that utilizing only M_1 data, the choice of the potential parameters for the excited state is by no means unique, as is evident from Fig. 10. We have calculated simultaneously both M_1, Eq. (4.13b), and M_2, Eq. (4.13c), utilizing the difference potential obtained from Eqs. (5.2) and (5.3) together with the appropriate $g_{11}(r)$ and $g_{12}(r)$ data, for a wide range of the excited state potential parameters. This procedure (see Fig. 10) conducted at several densities enabled us to derive the "best" potential parameters:

$$\epsilon = 0.008 \pm 0.002 \text{ eV} ,$$

$$r_e = 4.65 \pm 0.05 \text{ Å} , \qquad (5.4)$$

$$\alpha = 16 \pm 1 .$$

The error limit assigned to these potential parameters reflects their variation throughout the density range 0.3–1.4 g·cm^{-3} (see Sec. IV). In Fig. 11 we plot typical data for $V_g(R)$, $V_e(R)$, and $\Delta V(R)$. We note that the difference potential is dominated by the upper state potential which is much more repulsive than that of the ground state.

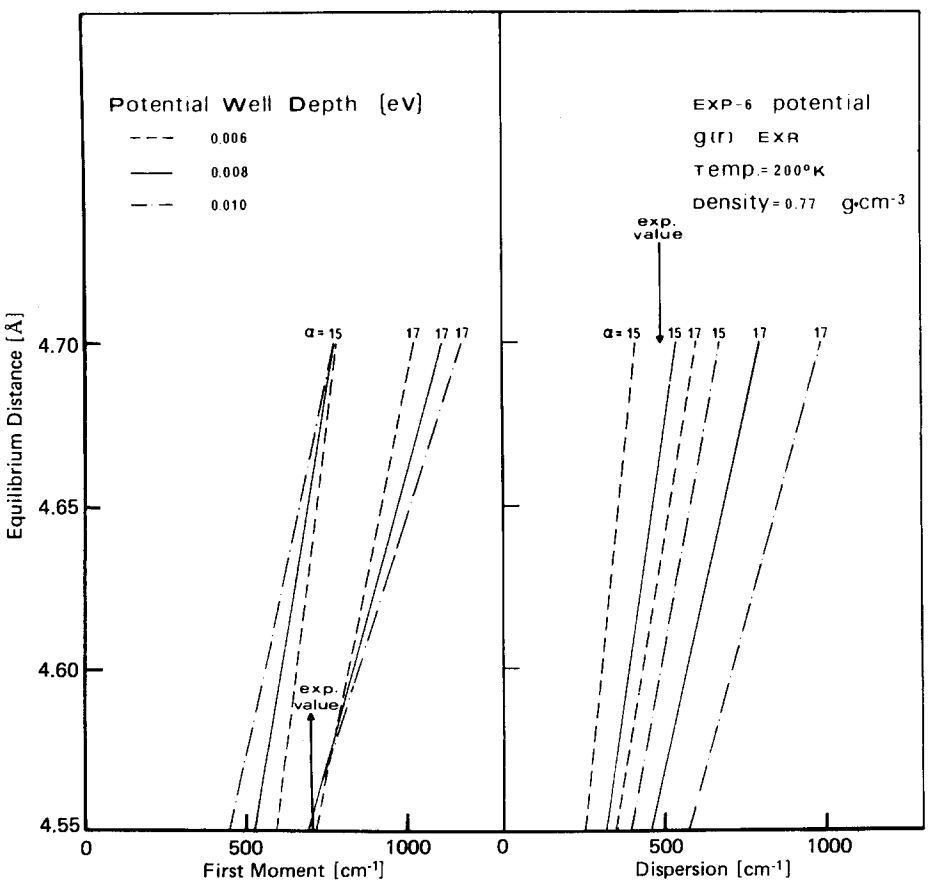

FIG. 10. The dependence of the calculated first moment and the spectral dispersion on the parameters of the exp – 6 excited state potential Eq. (5.3). These typical calculations are presented for $\rho = 0.77$ g·cm^{-3} at 200 °K using a RDF from x-ray data. Arrows designate the experimental values of M_1 and M_2.

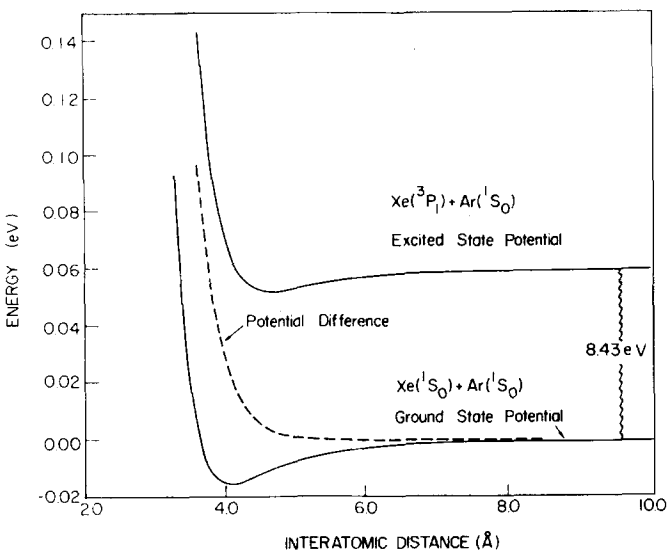

FIG. 11. Potential curves for $Xe(^1S_0)+Ar(^1S_0)$ potential, Eq. (5.2), $Xe(^3P_1)+Ar(^1S_0)$ excited state potential, Eqs. (5.3) and (5.4), and the difference potential $\Delta V(r)$ (dashed curve).

VI. SOLVENT SHIFTS IN THE Xe/Ar SYSTEM

We now proceed to a detailed analysis of our experimental data in terms of the semiclassical theory. The theoretical density dependence of M_1 and M_2 is portrayed in Figs. 12 and 13. These theoretical data were computed wherever RDF's for pure Ar are available. The first moment of the absorption band calculated in Fig. 12a with the potential parameters, Eq. (5.4), exhibits a weak temperature dependence in the range 260–100 °K in accord with our experimental results. These theoretical data reproduce quite faithfully the general density dependence of M_1 throughout the density region 0.3–1.4 g · cm^{-3}. The overall agreement at high ($\rho > 0.8$ g · cm^{-3}) densities is somewhat better using the exp-6 potential, Eq. (5.3), than the LJ potential for the excited state. Systematic deviations between theory and experiment are, however, exhibited in the lower density range $\rho = 0.3$–0.6 g · cm^{-3} and in the high density region $\rho = 1.1$–1.4 g · cm^{-3}. A slight modification of the potential parameters (within the uncertainty of those parameters) in these two density regions [see Fig. 12(b)] results in excellent agreement with the experimental data. We conjecture that this slight density dependence of the effective pair potential may reflect the contribution of three-body interaction terms to the potential energy, which were disregarded in the present treatment. However, we have to reserve judgment concerning this interesting point in view of the rather crude data for the two-component RDF's employed in the present calculations. The theoretical results for M_2 [Fig. 13(a)] again reproduce the gross features of the experimental data. In general, the predicted temperature dependence of M_2 is shown to be weak in accord with the experimental data in the temperature range 90–200 °K in the density range 0.6–1.4 g · cm^{-3}. The temperature dependence of M_2 in the low density ($\rho < 0.5$ g · cm^{-3}) range where M_2 decreases with increasing temperature may be tentatively accounted for in terms of the slight density dependence of the potential parameters (Fig. 13(b)).

Finally, it is important to assess the sensitivity of the calculated values of M_1 and M_2 to the nature of the

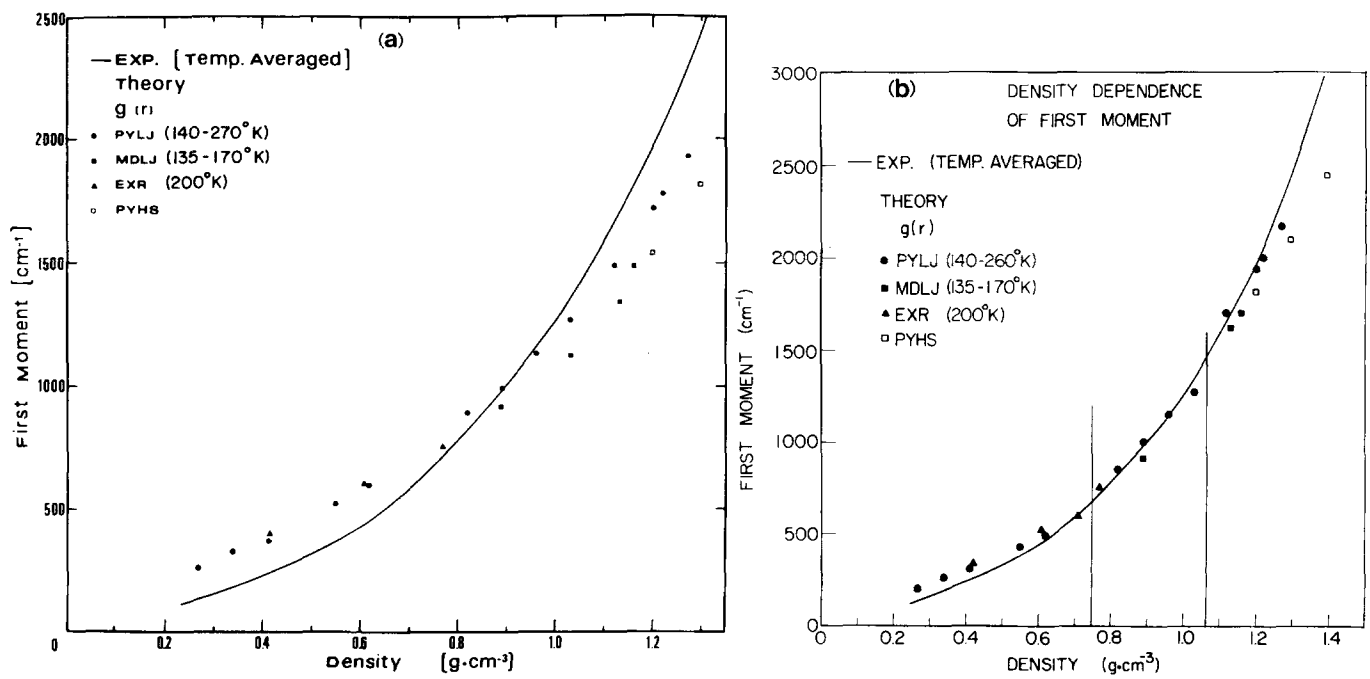

FIG. 12. (a) Density and temperature dependence of the first moment calculated from Eq. (4.13b) using the exp−6 excited state potential, Eq. (5.3), with the parameters $\epsilon = 8\times10^{-3}$ eV, $r_e = 4.65$ Å, $\alpha = 15$, together with all the available information on RDF's. Theoretical data designated by points while the solid curve represents the (averaged) experimental data. (b) Density and temperature dependence of the first moment calculated from the exp-6 excited state potential, Eq. (5.3), allowing for a slight density dependence of the potential parameters. $\rho = 0.1$–$0.75\,g\cdot cm^{-3}$: $\epsilon = 8\times10^{-3}$ eV, $r_e = 4.60$ Å, $\alpha = 15$. $\rho = 0.75$–$1.05\,g\cdot cm^{-3}$: $\epsilon = 8\times10^{-3}$ eV, $r_e = 4.67$ Å, $\alpha = 15$. $\rho = 1.5$–$1.4\,g\cdot cm^{-3}$: $\epsilon = 6\times10^{-3}$ eV, $r_e = 4.65$ Å, $\alpha = 17$. Presentation of theoretical and experimental data as in Fig. 12(a).

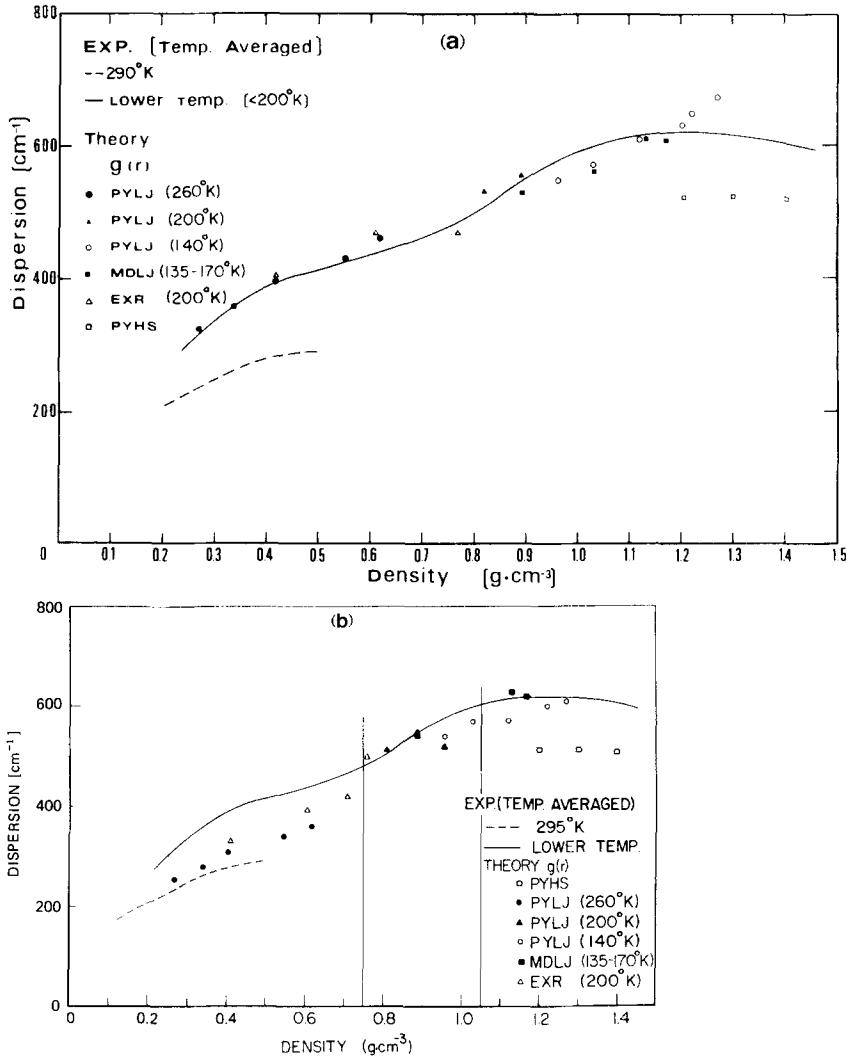

FIG. 13. (a) Density and temperature dependence of the spectral dispersion calculated from Eq. (4.13c) using the exp-6 excited state potential, Eq. (5.3), with the parameters used in Fig. 12(a), together with all the available information on RDF's. Theoretical data designated by points. The experimental data in the temperature range 90–200 °K are presented in terms of the solid curve, while the dashed curve represents the experimental results at 295 °K. (b) Density and temperature dependence of the spectral dispersion calculated from Eq. (4.13c) using the exp-6 excited state potential, Eq. (5.3), and allowing for a slight density dependence of the potential parameters as used in Fig. 12(b). Presentation of theoretical and experimental data as in Fig. 13(a).

RDF's employed herein. When physically reasonable RDF's extracted from theoretical MDLJ and PYLJ and from experimental EXR data are employed the calculated values of M_1 and M_2 are practically invariant to the nature of these RDF's. On the other hand, when more crude approximations for the RDF's are utilized the spectral perturbations are quite appreciably affected. Two observations are relevant in the context. First, using $g(r, T^*, \rho^*)$, Eq. (5.1), without scaling for $g_{12}(r, T, \rho)$ results in values of M_1 which are about 15% higher than those obtained from the scaled RDF, while the values of M_2 are practically unaffected. Second, the use of the rather crude PYHS RDF at high densities results in considerable deviations (see Figs. 12 and 13) from the values obtained using more refined RDF's.

The present theoretical treatment provides reliable estimates of the first and second moments of the absorption band. A calculation of the entire energy dependent line shape requires, in principle, not only the low order $A_1(t)$ and $A_2(t)$ terms in Eq. (4.8a) but also higher order terms. It is of some interest to evaluate the line shape, Eq. (4.5), at high densities for a hypothetical independent perturber model where the generating function, Eq. (4.6), is given by $f(t) = \exp[A_1(t)]$. To assess the role of three-body terms in the distribution function we have performed a calculation of the entire line shape, Eq. (4.5), using the generating function $f(t) = \exp[A_1(t) + A_2(t)]$. In Figs. 14(a)–14(c) we display the calculated line shapes for the independent perturber model and incorporating three-body correlation effects. We note that the three-body correlation effects are important already at moderate densities ($\rho = 0.4$ g · cm^{-3}) where the line shape is asymmetric, while at higher densities a substantial contribution to the (practically symmetric) line shape is provided. The experimental results also reproduced in Fig. 14 are in fair agreement (at least at high densities) with the line shape calculated when three-body correlation effects are incorporated.

In addition, a rough theoretical estimate of medium effects on the emission band[7] of Xe in liquid Ar was performed invoking the reasonable picture of solvent relaxation on a time scale which is considerably shorter than the radiative lifetime.[7,13] The first moment $\bar{M}_1$ and the dispersion $\bar{M}_2$ of the emission line are obtained from Eqs. (4.13b) and (4.13c) replacing $\Delta V(R)$ by $-\Delta V(R)$, taking for $g_{12}(R)$ the Percus–Yevick hard sphere RDF with $\sigma_{11} = 3.36$ Å and $\sigma_{12} = 4.3$ Å. This calculation results in $\bar{M}_1 = +300$ cm^{-1} and $\bar{M}_2 = 80$ cm^{-1}, at $\rho = 1.35$ g · cm^{-3}. The predicted spectral shift $\Delta_e \simeq \bar{M}_1$

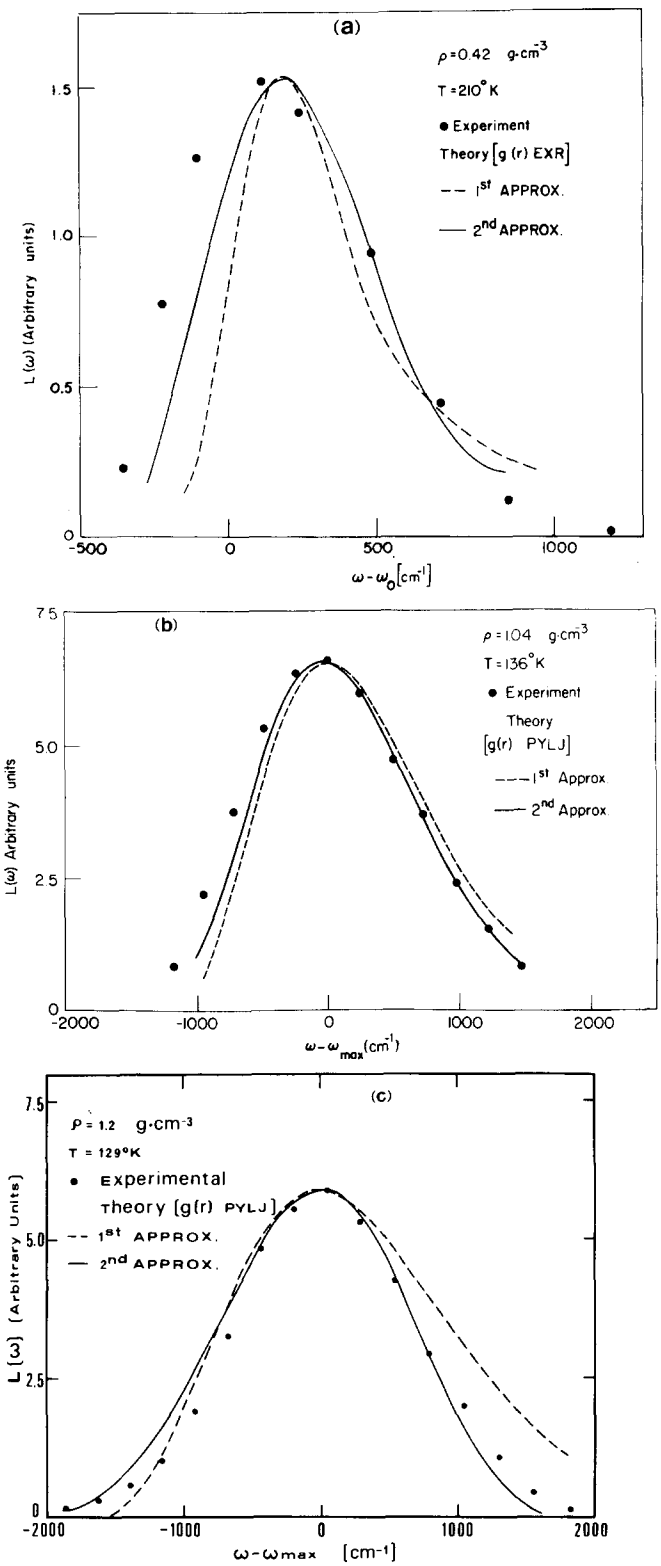

FIG. 14. Calculations of line shapes incorporating two-body and three-body correlation effects. The dashed curves are obtained using the generating function $f(t)=\exp(A_1(t))$, while the solid curves were calculated from $f(t)=\exp(A_1(t)+A_2(t))$, where $A_1(t)$ and $A_2(t)$ are given by Eq. (4.10a,b). The excited state potential is given by Eqs. (5.3) and (5.4). The points represent experimental data. (a) Low density data. $\hbar\omega_0=68\,045$ cm^{-1}. EXR RDF was employed. (b) Medium density data $\hbar\omega_{max}$ (experiment) $=69\,450$ cm^{-1}, $\hbar\omega_{max}$(theory) $=69\,250$ cm^{-1}. PYLJ RDF was employed. (c) High density data. $\hbar\omega_{max}$(experiment) $=70\,100$ cm^{-1}, $\hbar\omega_{max}$(theory) $=69\,950$ cm^{-1}. PYLJ RDF was employed.

$=+300$ cm^{-1} is very sensitive to the well depth in the excited state.[13] The experimental spectral shift in emission of Xe in liquid Ar[7a] ($\rho=1.35$ g·cm^{-3} $T=84$ °K) is $\Delta_e=-900\pm400$ cm^{-1}. We are not very much concerned with the discrepancy between theory and experiment in this case, in view of the inaccuracy involved in the rough estimate of $g_{12}(r)$. As pointed out by Saxton and Deutch,[13] the scaling method is not reliable in this case. More important, the rough estimate of $\bar{M}_1$ provides an adequate interpretation for the large Stokes shift in the emission of liquid Xe/Ar system. The calculated Stokes shift is $d=M_1-\bar{M}_1=3000$ cm^{-1} while the experimental value is $d=4000$ cm^{-1}. Thus a proper rationalization of the large Stokes shift and the small spectral shift in emission is provided. It is amusing to note that our more detailed calculations using a more elaborate excited state potential result in worse agreement between theory and experiment for the Xe/Ar emission spectrum than originally obtained by Saxton and Deutch.[13]

VII. CONCLUDING REMARKS

We assert that the semiclassical theory of line shapes provides a proper semiquantitative account for the weak temperature dependence and for the marked density dependence of the energetic parameters M_1 and M_2 specifying spectral shift and line broadening in the absorption spectra and the large Stokes shift in the emission of the Xe/Ar system. The semiclassical theory together with detailed absorption spectra can be utilized to extract quite reliable information concerning excited state potential curve. An alternative source of information[33] originating from spectral shifts and line broadening data involves the inverse process of using reliable ground state and excited state potentials, once the latter will become available, to extract structural information on the solution pair RDF. We have seen that the PYHS RDF's are not quite appropriate for fitting the spectral data at high densities, so that this approach is of interest for dense fluids. This procedure will be reliable only provided that the additivity assumption for the potential surfaces [see Eq. (4.3)] is sufficiently accurate. Another interesting avenue to pursue will be the use of accurate solution RDF's to assess the role of three-body interactions in determining spectral shifts.

We were able to elucidate the contributions of three-body atomic correlation effects to the line shape function. No attempt was made to estimate the effects of high order correlation (i.e., of order higher than 3), on the line shape. Instead, one can provide a general argument that once the experimental line shape function (at high densities) is Gaussian only two- and three-body correlation effects are important. The argument follows closely the theory of multiphonon processes in the strong coupling limit.[23] Utilizing Eqs. (4.8), and (4.13) then expanding $\ln f(t)$ in a power series we get

$$f(t)=\exp[i\alpha t-\beta t^2+O(t^3)]\,,$$
$$\alpha=m_1=M_1\,, \tag{7.1}$$
$$\beta=\tfrac{1}{2}(m_2-m_1^2)=\tfrac{1}{2}M_2^2\,.$$

When $\beta\gg1$ the generating (correlation) function decays

fastly to zero for sufficiently small values of t, whereupon the contribution of the $O(t^3)$ term is negligible. This situation is accomplished at high densities. We immediately note that four-body (and higher) atomic correlation effects appear in $O(t^3)$ and when the contribution of this term can be disregarded the high density spectrum is determined only by M_1 and M_2, i.e., by two-body and three-body correlations. The line shape is then to a good approximation

$$\mathfrak{L}(\omega) \propto \exp[(\omega - \omega_0 - M_1)^2/M_2] \qquad (7.2)$$

This Gaussian line shape constitutes a general high density result which, furthermore, is not confined to the semiclassical limit. As was demonstrated by Lax[24] and by Futrelle,[10b] the first and the second quantum mechanical moments for allowed optical transitions are given correctly by the semiclassical formulas. Our experimental absorption spectra at high densities ($\rho > 0.6$ g·cm^{-3}) are symmetrical and $\delta = (2.5 \pm 0.1)M_2$ providing a necessary condition for the line shape to be Gaussian. Unfortunately, our data are not sufficiently accurate (at high values of $\omega - \omega_{max}$) to establish whether the absorption line shape is indeed Gaussian in the high density range. Further high accuracy experimental data are required to establish this point.

The semiclassical theory successfully applied herein for Xe/Ar over a broad density ($\rho = 0.3$–1.4 g·cm^{-3}) range cannot be regarded as a unified theory of line shapes for this simple atomic system, as it is unable to account for the appearance of the blue satellites[19,20] at low densities (100–1000 torr Ar). In the low density range $\rho \to 0$ the line shape can be readily obtained from a power expansion of the generating function $\exp[A_1(t)]$ resulting in the well-known result[10,22]

$$\mathfrak{L}(\omega) = \rho \int \exp[-\beta V_g(R)]\, \delta[\hbar\omega - \hbar\omega_0 - \Delta V(R)]\, d^3R \ .$$

Red and blue satellites are then attributed[10,22] to minima and to maxima in the difference potential $\Delta V(R)$, respectively. In the case of Xe–Ar spectrum, the appearance of two blue satellites at low densities should infer relative maximum in the difference potential. This is not the case as is evident from the difference potential $\Delta V(R)$, Fig. 11, obtained by us from the analysis of the experimental data at higher ($\rho > 0.3$ g·cm^{-3}) densities, which is a smooth monotonically decreasing positive function of R. A more elaborate quantum mechanical treatment of the blue satellite bands in low density rare gas mixtures in terms of bound–continuum and continuum–continuum transitions between nuclear states of a guest–host pair is required.

ACKNOWLEDGMENTS

We are indebted to Professor J. M. Deutch for stimulating comments. This research was supported in part by the Nerken Foundation.

[1] G. Baldini, Phys. Rev. 137, 508 (1965).
[2] (a) A. Gedanken, B. Raz, and J. Jortner, Chem. Phys. Lett. 14, 172 (1972); (b) A. Gedanken, B. Raz, and J. Jortner, Chem. Phys. Lett. 14, 326 (1972); (c) A. Gedanken, B. Raz, and J. Jortner, J. Chem. Phys. 58, 1178 (1973).
[3] J. Jortner, in *Vacuum Ultraviolet Radiation Physics*, edited by E. E. Koch, R. Haensel, and C. Kunz, (Pergamon-Vieweg, Braunschweig, 1974) p. 263.
[4] B. Raz and J. Jortner, Proc. R. Soc. London Ser. A 317, 113 (1970).
[5] (a) J. Hermanson, Phys. Rev. 150, 660 (1967); (b) J. Hermanson and J. C. Phillips, *ibid.* 150, 652 (1967).
[6] (a) A. Gold, J. Phys. Chem. Solids 18, 218 (1961); (b) S. Webber, S. A. Rice, and J. Jortner, J. Chem. Phys. 42, 1907 (1965).
[7] (a) O. Cheshnovsky, B. Raz, and J. Jortner, J. Chem. Phys. 57, 4628 (1972); (b) A. Gedanken, B. Raz and J. Jortner, *ibid.* 59, 5471 (1973).
[8] (a) H. Margenau, Phys. Rev. 48, 755 (1935); (b) 82, 156 (1951); (c) H. Margenau and H. C. Jacobson, J. Quant. Spectrosc. Radiat. Transfer 3, 35 (1963); (d) F. Schuller and W. Behmenburg, Phys. Lett. Ser. C 12, 273 (1974).
[9] J. Robin, R. Bergeon, L. Galatry, and B. Vodar, Disscuss. Faraday Soc. 22, 30 (1956).
[10] (a) G. D. Mahan, Phys. Rev. A 6, 1273 (1972); (b) R. P. Futrelle, *ibid.* 5, 2162 (1972); (c) H. C. Jacobson, *ibid.* 4, 1363, 1368 (1971).
[11] J.-Y. Roncin, Chem. Phys. Lett. 3, 408 (1969).
[12] It is still an open question whether the assumption of substitutional disorder holds, and what is the contribution of inhomogeneous line broadening for impurity states in solid rare gases. The spectra of alkali atoms in solid rare gases [S. L. Kupferman and F. M. Pipkin, Phys. Rev. 166, 207 (1968)] are broad and diffuse, indicating either severe phonon coupling effects or inhomogenous broadening. On the other hand, the recent observation of zero-phonon, Shpolskii lines in the NO/Ne system [E. Boursey and J.-Y. Roncin, J. Mol. Spectrosc. 55, 31 (1971)] indicates that in this case the assumption of substitutional disorder is valid.
[13] M. J. Saxton and J. M. Deutch, J. Chem. Phys. 60, 2800 (1974).
[14] Xe($^3P_1$) designates the $6s[\frac{3}{2}]J=1$ state of the $5p^5(^2P^0_{3/2})6s$ configuration of atomic Xe according to C. E. Moore, Natl. Bur. Stand. (U.S.) Circ. 467 (1958).
[15] I. Messing, B. Raz, and J. Jortner, in *Vacuum Ultraviolet Radiation Physics*, edited by E. E. Koch, R. Haensel, and C. Kunz, (Pergamon-Vieweg, Braunschweig, 1974) p. 40.
[16] (a) R. E. Huffman, J. C. Larrabee, and Y. Tanaka, Appl. Opt. 4, 1581 (1965); (b) B. Raz, J. Magen, and J. Jortner, Vacuum 19, 571 (1969).
[17] From the ρ_2–P isotherm at room temperature (Ref. 18) we have constructed a ρ vs P curve for a given value of n. The intersection of the latter curve with the ρ–P isotherm for the temperature T (Ref. 18) results in the required value of ρ.
[18] A. L. Gosman, R. D. McCarty, and J. G. Hust, Natl. Bur. Stand. Ref. Data Ser. 27 (1969).
[19] (a) R. Granier, M.-C. Castex, J. Granier, and J. Romand, C. R. Acad. Sci. Ser. B 264, 778 (1967); (b) M.-C. Castex, R. Granier, and J. Romand, *ibid.* 268, 552 (1969).
[20] I. Messing, M. Sc. thesis, Tel Aviv University, Tel Aviv, 1970.
[21] J. M. Rupin, M. Morlais, and S. Robin, C. R. Acad. Sci. Ser. B 265, 1177 (1967).
[22] For a recent review of gas phase line broadening resting on the evaluation of Franck–Condon factors see J. Szudy and W. E. Baylis, J. Quant. Spectrosc. Radiat. Transfer 15, 641 (1975).
[23] R. Kubo and Y. Toyozawa, Prog. Theoret. Phys. Japan 13, 160 (1955).
[24] M. Lax, J. Chem. Phys. 20, 1752 (1952).
[25] J. K. Percus in *Classical Fluids*, edited by H. L. Frisch and S. L. Lebowitz (Benjamin, New York, 1964).
[26] M. Born and A. S. Green, Proc. R. Soc. London Ser. A 188, 10 (1946).

[27]G. J. Throop and R. J. Bearman, J. Chem. Phys. 42, 2408 (1965).
[28]G. J. Throop and R. J. Bearman, J. Chem. Phys. 42, 2838 (1965).
[29]L. Verlet, Phys. Rev. A 6, 1273 (1968).
[30]F. Mandel, R. J. Bearman, and M. Y. Bearman, J. Chem. Phys. 52, 3315 (1970).
[31]Mikolaj and Pings, J. Chem. Phys 46, 1412 (1967).
[32]W. Hogervorst, Physica, (Utrecht) 51, 90 (1971).
[33]J. M. Deutch (private communication).